

Model-based analysis of cortical recording with silicon microelectrodes

Michael A. Moffitt, Cameron C. McIntyre*

Department of Biomedical Engineering, Cleveland Clinic Foundation, Lerner Research Institute,
ND-20, 9500 Euclid Avenue, Cleveland, OH 44195, USA

Accepted 22 May 2005

Abstract

Objective: The purpose of this study was to use computational modeling to better understand factors that impact neural recordings with silicon microelectrodes used in brain–machine interfaces.

Methods: A non-linear cable model of a layer V pyramidal cell was coupled with a finite-element electric field model with explicit representation of the microelectrode. The model system enabled analysis of extracellular neural recordings as a function of the electrode contact size, neuron position, edema, and chronic encapsulation.

Results: The model predicted spike waveforms and amplitudes that were consistent with experimental recordings. Small ($< 1000 \mu\text{m}^2$) and large ($10\text{k} \mu\text{m}^2$) electrode contacts had similar volumes of recording sensitivity, but small contacts exhibited higher signal amplitudes ($\sim 50\%$) when neurons were in close proximity ($50 \mu\text{m}$) to the electrode. The model results support the notion that acute edema causes a signal decrease ($\sim 24\%$), and certain encapsulation conditions can result in a signal increase ($\sim 17\%$), a mechanism that may contribute to signal increases observed experimentally in chronic recordings.

Conclusions: Optimal electrode design is application-dependent. Small and large contact sizes have contrasting recording properties that can be exploited in the design process. In addition, the presence of local electrical inhomogeneities (encapsulation, edema, coatings) around the electrode shank can substantially influence neural recordings and requires further theoretical and experimental investigation.

Significance: Thought-controlled devices using cortical command signals have exciting therapeutic potential for persons with neurological deficit. The results of this study provide the foundation for refining and optimizing microelectrode design for human brain–machine interfaces.

© 2005 International Federation of Clinical Neurophysiology. Published by Elsevier Ireland Ltd. All rights reserved.

Keywords: Cortical recording; Neural recording; Computational model; Brain–machine interface; Microelectrode

1. Introduction

Brain–machine interfaces represent an emerging area of neurotechnology with both basic science and clinical applications. The development of silicon-substrate microelectrode arrays has enabled chronic recording of single-unit activity from multiple neurons simultaneously, opening the door for exciting experimental and therapeutic possibilities. Recordings with microelectrode arrays are used to better understand the organization and processing strategies of the nervous system (Buzsaki, 2004; Csicsvari et al., 2003). One promising clinical application is the use of

cortical recordings as command signals for thought-controlled devices that benefit impaired individuals (Kennedy et al., 2004; Nicolelis and Chapin, 2002; Taylor et al., 2002), and the first human clinical trial has begun utilizing high-density silicon microelectrode technology (Serruya et al., 2004). However, a number of neurophysiology and engineering questions remain to be addressed before these types of electrodes can be truly optimized for specific clinical and experimental objectives.

There exists a long history of experimental and theoretical investigations of factors influencing single unit extracellular recordings (Rall, 1962). Recently, Holt and Koch (1999) provided a detailed description of the amplitude and spike waveform generated by layer V cortical pyramidal neurons recorded with a point electrode

* Corresponding author. Tel.: +1 216 445 3264; fax: +1 216 444 9198.
E-mail address: mcintyc@ccf.org (C.C. McIntyre).

in an infinite, homogeneous, isotropic medium. Their results represent an initial foundation for analysis of cortical microelectrode recordings; however, some fundamental questions remain. For instance, it is presently unclear how neural signals are influenced by the size of the electrode contact, which range from hundreds to thousands of square microns in surface area (Csicsvari et al., 2003; Cui et al., 2001; Vetter et al., 2004). Second, the effects of local tissue changes (e.g. acute edema or chronic tissue encapsulation) have been difficult to quantify and both signal increases and signal decreases over time have been observed experimentally (Vetter et al., 2004; Williams et al., 1999). The purpose of this study was to use computational modeling to better understand factors expected to impact neural recording. In particular, we examined the effects of contact size, neuron-to-contact position, and local electrical inhomogeneities. Outcome measures were the amplitude and shape of the computed waveform, and the volume of recording sensitivity. Computational methods included a cable model of a layer V pyramidal cell and finite-element volume conductor model of the microelectrode and surrounding medium, which were coupled through an efficient reciprocity-based approach.

The coupled neuron-field model was able to simulate recorded waveforms with shapes and amplitudes comparable to those observed experimentally. The results of the study indicated that contact sizes between 200 and 1000 μm^2 yield only slightly different recording amplitudes ($\sim 8\%$) and the waveforms had comparable shapes. A large contact size (10k μm^2) resulted in a reduced signal amplitude ($\sim 51\%$), but a more uniform volume of recording sensitivity. The model results support the notion that acute edema causes a signal decrease ($\sim 24\%$), and interestingly, that certain encapsulation conditions can result in increased signal amplitude ($\sim 17\%$), a mechanism that may contribute to signal increases observed experimentally (Vetter et al., 2004). Extensions of these analyses will enable development of silicon-substrate microelectrodes with optimized contact size, shape, and distribution to achieve specific recording objectives.

2. Methods

The computational model of neural recording consisted of two major components: an electrical volume conductor model and an electrical source model. The electrical volume conductor was a finite element model (FEM) of the head with the implanted microelectrode. The electrical source was a multi-compartment cable model of a neuron that provided a time-dependent description of the transmembrane currents generated during action potential signaling.

2.1. Electrical volume conductor model

A finite-element model (FEM), with dimensions representative of the rat head, was developed with ANSYS 8.0 (Ansys, Inc., Canonsburg, PA), and included explicit representation of a silicon microelectrode (Fig. 1A). The rat head was modeled as 4 concentric spheres representing the brain, cerebrospinal fluid (CSF), skull, and scalp with radii of 8000, 8500, 9000, and 10,000 μm , respectively. The diameter of the head and the thickness of the scalp and skull layers were estimated from a previously described rat head model (Ogiue-Ikeda et al., 2003) and the thickness of the CSF was estimated from images of rat head and spinal cord acquired in other studies (Franconi et al., 2000; Liu et al., 2004; Thorsen et al., 2003).

The microelectrode consisted of a shank that was 15 μm thick, 107 μm wide, and 2700 μm long, similar to those used in practice (Vetter et al., 2004). Square-shaped contact domains were positioned on the shank at a depth of 2000 μm below the CSF–brain interface, and were arranged such that a contact size of 200, 400, 800, 1000, or 10k μm^2 could be selected (Fig. 1B). Sheath domains were created immediately adjacent to the electrode so that local electrical inhomogeneities (e.g. edema or encapsulation) could be modeled with thicknesses of 10, 20, or 30 μm , comparable to observed encapsulation thicknesses (Szarowski et al., 2003; Turner et al., 1999).

The electrical parameters of the head model domains were the same as those used in a previously published head model (Hauelsen et al., 2002), and are given in Table 1. In simulations of chronic encapsulation, the default resistivity of the sheath was taken from a peripheral nerve encapsulation study (Grill and Mortimer, 1994) and was varied in a sensitivity analysis in this study (Table 1). Similarly, in simulations of acute edema, the sheath resistivity was half the resistivity of gray matter, and was also reduced to the resistivity of CSF in a sensitivity analysis.

The model was discretized in space using tetrahedral elements (ANSYS element SOLID98) (Fig. 1C) that consisted of 10 nodes, one node on each of the 4 vertices, and an additional bisector node on each of the 6 edges. The model consisted of over 900,000 nodes, with over 290,000 nodes in a region-of-interest (ROI) that contained the electrode and brain tissue in a $300 \times 300 \times 300 \mu\text{m}$ box surrounding the electrode contact. Adjacent nodes (one-half of a tetrahedral edge length) were required to be $\leq 5 \mu\text{m}$ apart in the ROI, $\leq 50 \mu\text{m}$ in a 200 μm thick shell surrounding the ROI, $\leq 1.625 \text{ mm}$ in the remaining medium.

Load and boundary conditions were necessary to achieve a model solution. The load condition consisted of an ideal point current located at the electrode contact (reciprocal solution—rationale described below). The boundary condition required the voltage on the bottom of the head (the side opposite the electrical source) to attenuate to zero,

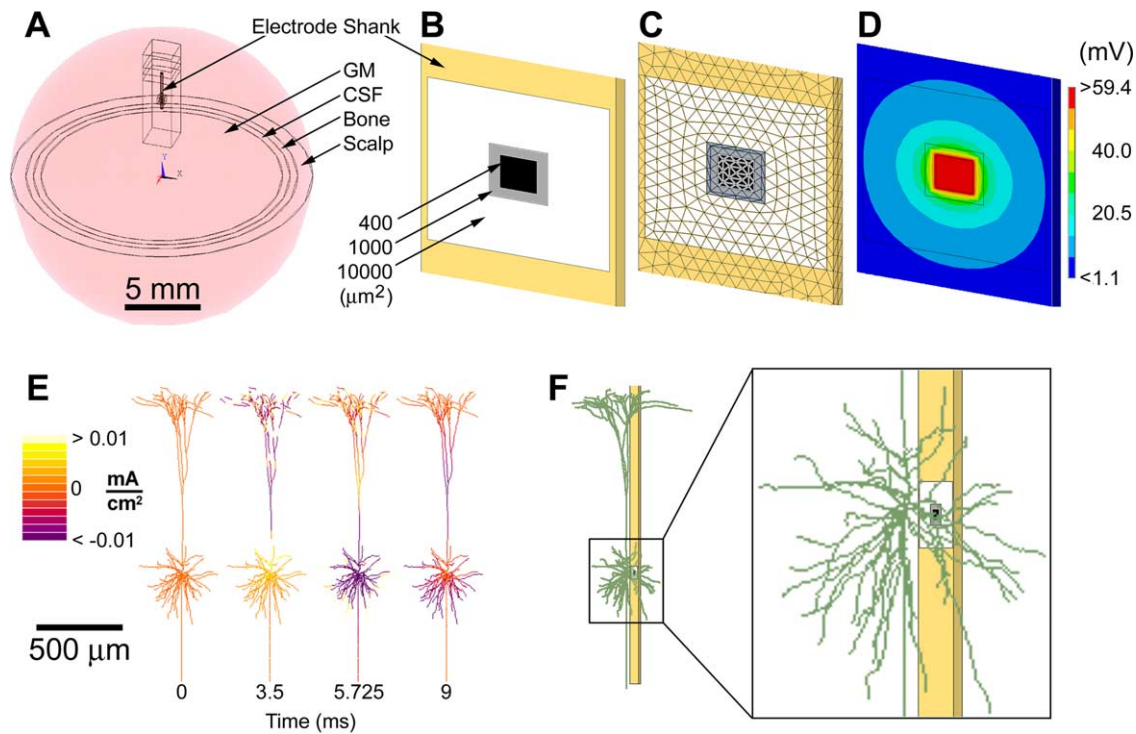


Fig. 1. Computational model of neural recording. Neural recordings were generated by coupling a volume conductor head model (A–D) and a cable-style neuron model (E, F). The head model (A) consisted of 4 concentric sphere representing the gray matter (GM), cerebrospinal fluid (CSF), bone, and scalp. Within the gray matter, domains representing the electrode shank and several contact sizes were defined. A close-up view of contact domains (B), the finite-element mesh (C), and an example field model solution (D) are depicted. (E) The cable model of the layer V pyramidal cell and the current density at 4 time points spanning an action potential evoked by synaptic activation of the apical dendritic tuft. (F) Pictorial representation of the neuron with the soma positioned 50 μm from the electrode contact.

consistent with attenuation that would be observed on an electroencephalogram (EEG) for a distant source. The electrostatic model was solved in ANSYS with an iterative Jacobi conjugate gradient solver.

2.2. Electrical source model (layer V pyramidal cell)

The neuron model used in this study was based on a cable model of a layer V pyramidal cell from cat visual cortex described previously (Mainen et al., 1995; Mainen and Sejnowski, 1996) and is depicted in Fig. 1E. No modifications were made to the ion channel properties of

the original model. Geometric modifications included extension of the 5 node/5 internode axon to a 20 node/20 internode axon that extended from the soma downward (i.e. away from the pial surface). Further, dendritic compartments that intersected with the electrode when the neuron was 50 μm away, and their children compartments, were removed (38 of 438 dendritic compartments removed), to avoid having neuronal sources within the electrode shank. The orientation of the neuron was adjusted to reduce the number of sections that had to be removed. NEURON 5.4 (Hines and Carnevale, 1997) was used to determine transmembrane currents as a function of time for each of the 531 compartments of the active neuron, and these transmembrane currents comprised the electrical source that was applied to the volume conductor model. Excitation was induced by applying a synaptic current to each dendritic branch in the apical tuft (60 branches), using the alpha synapse mechanism in NEURON as described by the equations below:

$$I_{\text{syn}}(t) = g(t)(V_m(t) - E_{\text{rev}})$$
 (1)

$$g(t) = \frac{g_{\text{max}}t}{\tau} e^{-(t-\tau)/\tau}$$
 (2)

where I_{syn} is the synaptic current, V_m is the transmembrane potential, and the parameters of the synaptic input, E_{rev}

Table 1
Electrical properties of field model domains

Domain	Resistivity ($\Omega\text{ cm}$)
Brain (gray matter)	300
Cerebrospinal fluid	56
Skull	16,000
Scalp	230
Encapsulation	600 ^a [600,6000] ^b
Edema	150 ^c [56,150] ^b
Electrode shank	100,000,000
Electrode contact	0.000025

^a Default encapsulation resistivity.
^b Range used in sensitivity analyses.
^c Default edema resistivity.

(0 mV), g_{\max} (10 nS), and τ (1 ms), were set to be representative of a strong AMPA-type excitatory input. Transmembrane currents were recorded for 12 ms (steps of 25 μ s) and spanned a single action potential.

2.3. Extracellular neural recording: theory

In the coupled neuron-FEM model, the neuron is represented as a set of point currents (531 transmembrane currents computed in NEURON) at the appropriate spatial locations in the FEM model, and the voltage at the contact is computed. This process is repeated for each time step of the neuron simulation to calculate the recorded voltage waveform at the electrode.

It is convenient to describe the solution to the coupled neuron-FEM model as a matrix equation. The fundamental computational task is to calculate the voltage impressed on the electrode contact for a unit current at an arbitrary point in the volume conductor. The magnitude and sign of the point current can be modified by multiplicative scaling, and the solutions from multiple point currents can be summated to create the neuron model that consists of 531 point currents. Further, the recorded voltage at different time instances is easily computed by changing the scale factors corresponding to each point source. Mathematically, we formulate the problem as the following matrix equation

$$\Phi(1 \times t) = K(1 \times n)J(n \times t) \quad (3)$$

where Φ is a $(1 \times t)$ vector containing the voltage at the contact at t instances in time, K is a $(1 \times n)$ vector that contains the voltage impressed on the contact for a unit current at each of the n spatial positions corresponding to compartments of the neuron model, and J is an $(n \times t)$ matrix that contains the scale factors for each point current of the neuron model and at each instance in time.

While J is computed directly in NEURON, K must be derived from the FEM model. Computation of K by direct application of the point currents to the FEM is not practical, because point currents can only exist at mesh nodes in ANSYS. Further, a separate solution of the finite-element model would be required for each of the n current sources in the model using the direct approach.

An alternative reciprocity-based approach utilizes a single reciprocal FEM solution (theorem of reciprocity (Helmholtz, 1853)) and subsequent interpolation to compute K . The reciprocal solution is generated by placing a current source at the electrode contact and solving for the scalar potential in the volume conductor. By the theorem of reciprocity (Helmholtz, 1853), the output voltage at a given node in the finite element mesh can be interpreted as the voltage that would be impressed on the electrode contact for a unit current at that node. The voltage at the contact due to unit currents at arbitrary positions (i.e. the elements of K) is solved by interpolation, based on the known values at the nodes that comprise the reciprocal FEM solution. In this

study, linear interpolation was performed in Matlab (The Mathworks, Inc.).

2.4. Extracellular neural recording: data collection

The effect of model complexity was analyzed by comparing simulated recordings for 4 models of increasing complexity: (1) an analytical model that assumed a zero area point electrode and an infinite homogenous isotropic medium ($\rho = 300 \Omega \text{ cm}$); (2) a FEM that included the head representation and a point electrode in the gray matter, but no explicit electrode shank, (3) a FEM that included the head and a point electrode on an explicit electrode shank, and (4) a FEM with the head, shank, and a finite-size microelectrode contact explicitly represented. Voltage records were simulated for several neuron-to-electrode positions, where the soma was translated in the direction normal to the contact (range = [50, 150 μ m]), and in the direction parallel to the shank (range = [−200, 200 μ m]). Further, to analyze the effect of contact-size, multiple contact sizes were used (point, 400, 1000, and 10k μm^2) and the peak-to-peak voltage was computed as a function of distance from the contact.

The effect of local resistivity decreases (resulting from edema) and increases (resulting from tissue encapsulation) was analyzed in the model. Encapsulation thicknesses around shanks were estimated to be tens of microns (range = [10, 30 μ m]) (Szarowski et al., 2003; Turner et al., 1999), and the effect of the resistivity of the encapsulation layer was examined in a sensitivity analysis (range = [300, 6000 $\Omega \text{ cm}$]). Acute edema was modeled as a 20 μ m thick layer of reduced resistivity around the electrode shank, and the value of the resistivity was examined through sensitivity analysis (range = [56, 300 $\Omega \text{ cm}$]).

The reciprocal FEM solution can also be interpreted as the sensitivity of the recording electrode to monopolar point currents in space (Rush and Driscoll, 1969). This interpretation was used to visualize changes in the spatial recording sensitivity under various experimental conditions. The volumes of monopolar recording sensitivity were computed and plotted for default, edema, and encapsulation conditions, and the effect of the local inhomogeneities was quantified as the percent change (from default) in recording sensitivity. Voltage records were simulated and compared, and peak-to-peak voltages were quantified and used in the sensitivity analyses.

3. Results

3.1. Limitations of analytical models

An objective of this study was to assess the effect of the complexity of the volume-conductor model on simulated voltage records due to the presence of an active neuron. Records simulated with several models and for several neuron positions are plotted in Fig. 2. Simulated records for

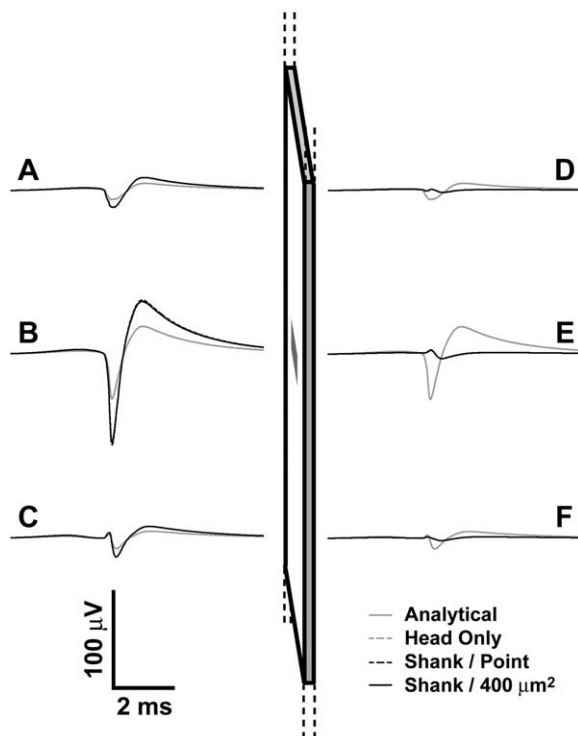


Fig. 2. Effects of model complexity on neural recordings. Extracellular recordings with 4 models: (1) an analytical model of a point electrode in an infinite homogenous isotropic medium ($\rho=300 \Omega \text{ cm}$) (solid gray lines), (2) a model that included the head representation but no explicit shank and a point electrode in the gray matter (dashed gray lines), (3) a model that included the head and a point electrode on an explicit shank (dashed black lines), and (4) a model with the head, shank, and a $400 \mu\text{m}^2$ contact explicitly represented (solid black lines). Simulations were run with the soma of the neuron $65 \mu\text{m}$ from the contact and either $100 \mu\text{m}$ above (A), centered (B), or $100 \mu\text{m}$ below (C) the contact, and corresponding positions on the opposite side of the shank (D–F). Note that the simulated recordings of the two models without a shank (gray lines) nearly overlap, as do the simulated recordings of the two models with a shank (black lines). Also, the simulated recordings without a shank are identical on both sides of the contact, in contrast to the ‘shadowing’ effect observed when the shank is present.

4 models (see Section 2) were plotted, and the results showed that the two models that did not explicitly represent the shank produced nearly overlapping waveforms, as did the two models where the shank was explicitly represented. On the contact-side of the shank (Fig. 2A–C), the simulated voltage records from all 4 models had a similar shape, but models that included a shank produced voltage records with a higher magnitude (77–100% increase). The similarity in shape on the contact side of the shank indicated that the same neural elements were contributing to the simulated signal in each of the 4 models. On the side of the shank opposite to the contact (Fig. 2D–F), the presence of the shank yielded very small records ($3.6\text{--}8.4 \mu\text{V}$) compared to simulations with the shank absent ($16\text{--}72 \mu\text{V}$). When the neuron was within $65 \mu\text{m}$ of the electrode shank and at the appropriate depth but on the side opposite to the contact (Fig. 2E), the models that did not incorporate the shank

over-estimated the peak-to-peak voltage by a factor of 8.5. Further, the polarities of the phases of the waveforms were switched (Fig. 2E), indicating that the dendrites played a larger role in the shape of the simulated waveform (see inset of Fig. 3) when the soma was on the side of the shank opposite to the contact. In the models that did not include a representation of the shank, the voltage records were similar on both sides of the electrode, i.e. no ‘shadowing’ from the shank was observed.

3.2. Effect of neuron-to-electrode position

The coupled neuron–FEM model was used to simulate voltage records for several neuron-to-electrode positions (Fig. 3). Consistent with experimental observations (Vetter et al., 2004), the simulated waveforms were typically biphasic (Fig. 3B–F, J–K), although other simulated waveforms with additional phases were observed at some neuron positions (Fig. 3G–I). Inward currents at the hillock and initial segment resulted in a negative phase that was followed by a positive phase caused by outward somatic currents (Fig. 3 inset, transmembrane currents) (Holt and Koch, 1999). The dendritic currents tended to be outward during the negative phase and inward during the positive phase (Fig. 3 inset, transmembrane currents), and had the effect of reducing the amplitude of the waveform (data not shown) (Holt and Koch, 1999).

The peak-to-peak amplitude of simulated recordings was plotted as a function of the neuron-to-electrode position (Fig. 4). In the vertical direction (parallel to the electrode shank) (Fig. 4 top), the maximum peak-to-peak amplitude ($\sim 200 \mu\text{V}$ for contacts $\leq 1000 \mu\text{m}^2$) was observed when the soma was immediately in front of the electrode contact, and dropped below $50 \mu\text{V}$ when the soma was $\sim 80 \mu\text{m}$ above or below the contact. However, at each vertical test site the soma was $50 \mu\text{m}$ from the shank, so the total neuron-to-contact distance was $\sim 100 \mu\text{m}$ when recording amplitudes dropped below $50 \mu\text{V}$. Note also that the decrease in amplitude in the vertical direction was symmetric about the level of the contact.

The peak-to-peak amplitude of simulated recordings was also plotted for neuron positions along a line normal to the face of the electrode contact (Fig. 4, bottom). Maximum amplitudes were observed when the soma was nearest to the contact, and decreased as the soma was moved away from the contact, again dropping below $50 \mu\text{V}$ at a neuron-to-contact distance of $\sim 100 \mu\text{m}$.

3.3. Effect of contact size

The coupled neuron–FEM model was used to simulate voltage records with several contact sizes (Figs. 3 and 4). Small contact-sizes ($\leq 1000 \mu\text{m}^2$) resulted in nearly overlapping simulated recordings (data not shown). The peak-to-peak amplitudes computed with the $400 \mu\text{m}^2$

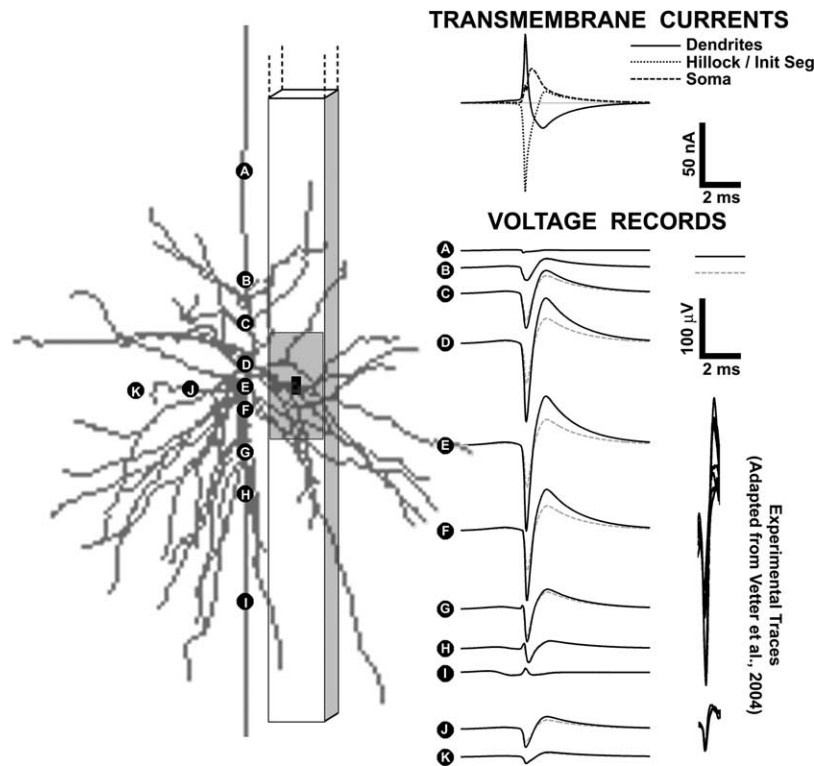


Fig. 3. Effects of contact size and neuron position on recorded waveforms. Pictorial representation of the neuron and electrode geometry is shown on the left. Eleven neuron-electrode positions were used in the simulations. For each simulation, the soma of the neuron was positioned at a corresponding letter (A–K). The explicit neuron-electrode geometry is drawn for simulation (E). Extracellular voltage recordings for each of the neuron-electrode positions (A–K) were calculated with either a $400\ \mu\text{m}^2$ (solid black lines) contact or a $10\text{k}\ \mu\text{m}^2$ contact (dashed gray lines). A–I are collinear $50\ \mu\text{m}$ from the shank and have vertical positions of 200, 100, 60, 20, 0, -20 , -60 , -100 , and $-200\ \mu\text{m}$, respectively. E, J, and K are 50, 100, and $150\ \mu\text{m}$ from center of the contact along a line normal to the contact face. Experimental traces from Fig. 5 of Vetter et al. (2004) are plotted to their right. Note that both experimental and simulated waveforms have a biphasic (negative first) shape and are of comparable amplitudes. The transmembrane currents from all compartments pertaining to either the soma, the hillock and initial segment, or the local dendritic arbor (apical tuft not included) were summed and are plotted (inset top right) (inward current = down) to illustrate their contributions to the extracellular recordings.

contact were $\sim 5\%$ less than amplitudes computed with an infinitesimal point contact, and $\sim 6\%$ greater than amplitudes computed with the $1000\ \mu\text{m}^2$ contact (Fig. 4). When a large contact ($10\text{k}\ \mu\text{m}^2$) was used, the peak-to-peak amplitude was $\sim 50\%$ smaller than when the $1000\ \mu\text{m}^2$ contact was used, at neuron positions near the contact (Figs. 3D–F and 4). However, the $10\text{k}\ \mu\text{m}^2$ contact had a more uniform volume of recording sensitivity, i.e. the peak-to-peak amplitude did not decrease as rapidly with increased neuron-to-contact distance as observed with the smaller contact sizes (Fig. 4). At neuron-to-contact distances $\geq 100\ \mu\text{m}$, the peak-to-peak amplitudes computed with the $400\ \mu\text{m}^2$ and the $10\text{k}\ \mu\text{m}^2$ contacts were comparable (Fig. 3, positions A, B, H, I, K).

3.4. Effect of local conductivity changes (encapsulation/acute local edema)

Maps of the electrode recording sensitivity to a monopolar point source are depicted in Fig. 5 for the default condition (no sheath around electrode) (Fig. 5A), for

a $20\ \mu\text{m}$ thick encapsulating layer (Fig. 5B₁), and for a $20\ \mu\text{m}$ thick layer of edema (Fig. 5B₂). Differences in the recording sensitivity as a function of space are readily apparent in maps of the percent change in recording sensitivity, and indicate that current sources on the side of the contact will have a higher recording amplitude when encapsulation is present than in the default condition (Fig. 5C₁), and a lower recording amplitude when edema is present (Fig. 5C₂). In the coupled neuron–FEM model, the peak-to-peak amplitude increased 17% when encapsulation was included in the model (compared to the default condition) and decreased 24% when edema was included in the model (Fig. 5D).

Peak-to-peak amplitude of the simulated recordings was sensitive to the thickness of the encapsulation layer, particularly at lower values, and continued to increase as the thickness increased (Fig. 6 top) over the range examined ($[0, 30\ \mu\text{m}]$). The peak-to-peak amplitude was also sensitive to the resistivity of the sheath layer (Fig. 6 bottom). In the coupled neuron–FEM model, the peak-to-peak amplitude at first increased with increasing resistivity, then began to decrease at a value between 600 and $3000\ \Omega\text{cm}$ (Fig. 6 bottom, solid black line).

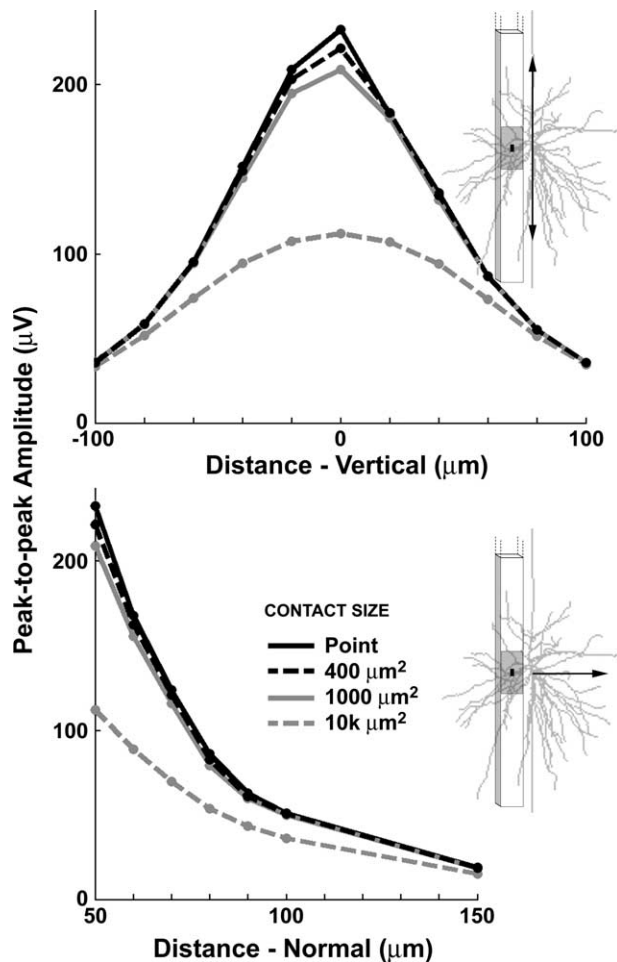


Fig. 4. Effects of contact size and neuron position on signal amplitude. Peak-to-peak amplitudes of neural recordings were collected as a function of distance of the neuron from the electrode contact. Electrode contact size ranged from an infinitesimal point on the electrode shank to a $10\text{ k } \mu\text{m}^2$ surface area contact. In the top plot, the vertical position of the neuron ranged from 100 below to 100 μm above the center of the contact along a line parallel to and 50 μm from the shank (same range as B–H of Fig. 3). In the bottom plot, the neuron positions were along a line normal to and through the center of the contact face and ranged from 50 to 150 μm from the contact (same range as E, J, K of Fig. 3).

However, when the effect of current sources inside the encapsulation layer (7 of the 531 neuron compartments pertained to dendrites inside the encapsulation layer) was removed, the peak-to-peak amplitude always increased as the resistivity increased (Fig. 6 bottom, dashed black line).

4. Discussion

4.1. Consistencies with experimental results

We used coupled neuron–FEM models to evaluate the limitations of analytical models of neural recording and to analyze the effects of neuron-to-contact position, contact-

size, and local electrical inhomogeneities on neural recordings. The model was able to reproduce several experimental observations, lending confidence to the conclusions and predictions of the present study. First, the model reproduced the standard biphasic extracellular recording waveform (negative phase first) most frequently observed experimentally (Henze et al., 2000; Vetter et al., 2004; Williams et al., 1999). Second, although difficult to directly compare, the recording amplitudes predicted by the model were consistent with the amplitudes of experimental recordings with silicon shank electrodes (Csicsvari et al., 2003; Henze et al., 2000; Vetter et al., 2004). Finally, the model-predicted relationship between the extracellular and intracellular (somatic) recordings (data not shown) was consistent with conclusions derived from experimental observations (Henze et al., 2000). In particular, the model and experimental results showed that the initial extracellular and intracellular deflections were coincident, the extracellular waveform peaked before the intracellular waveform, and the peak of the extracellular positive phase was nearly coincident with the end of the intracellular spike (Fig. 1 of Henze et al., 2000).

4.2. Limitations of analytical models

An objective of this study was to determine under what conditions an analytical model of neural recording is sufficient and when a more complex model is required. Our results indicate that an analytical model is adequate for predicting the shape of the extracellular waveforms that would be recorded when a neuron is on the contact-side of a silicon shank (Fig. 2A–C), but underestimates the amplitude by a factor of 1.75–2. The models that explicitly represented the electrode shank also showed a ‘shadowing’ effect on the side of the shank opposite to the contact (Fig. 2D–F) that resulted in different waveforms and vastly different (factor of ~ 8.5) amplitudes (Fig. 2E). Finally, analyses of contact-size (Fig. 3), changes in the local electrical environment (Figs. 5–7), and other factors of neural recording require a model that permits inhomogeneous domains of arbitrary shape.

4.3. Volume of recording sensitivity

A useful feature of computational models like those used in this study is that they can estimate the volume of recording sensitivity for an arbitrary electrode design. A volume of recording sensitivity for silicon shank electrodes was estimated by comparing experimentally observed recording amplitudes (average = 50–100 μV ; range = [50, 800 μV] (Vetter et al., 2004)) to model-predicted amplitudes as a function of neuron-to-contact distance. The model predicted that a 50 μV signal (low end of experimental range) will be observed when the neuron is ~ 100 μm from the contact, and is on the same side of the shank as the contact. Experimental validation of these results would be

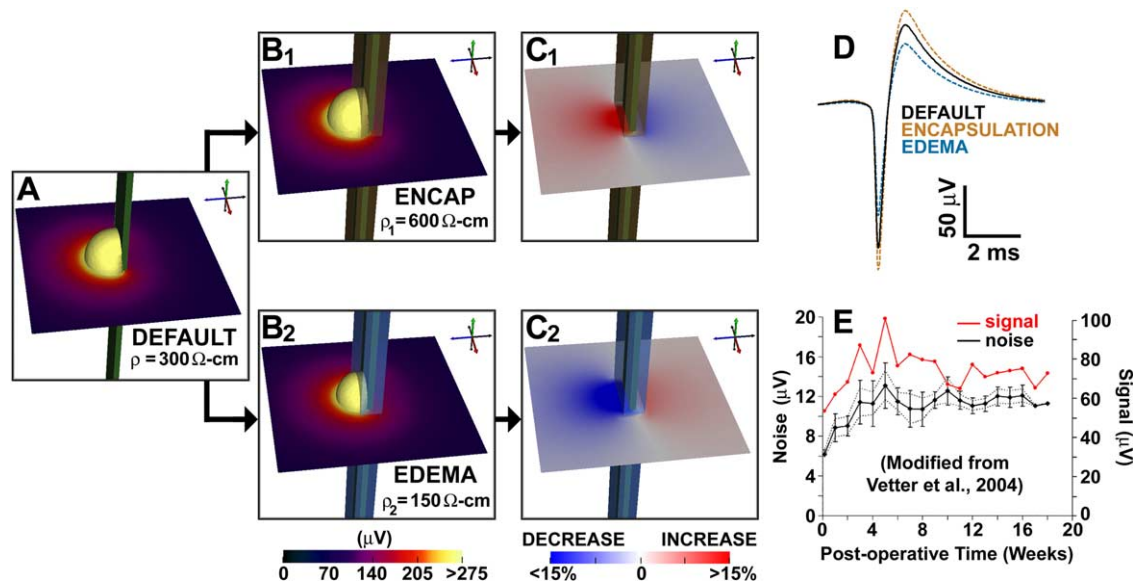


Fig. 5. Effects of local electrical inhomogeneities on neural recordings. False-color maps of electrode sensitivity to a monopolar source (i.e. reciprocal solutions) to models with no sheath around the electrode (A), an encapsulation sheath (B₁), and a sheath representing edema (B₂) are depicted. These maps can be interpreted as the voltage that would be impressed on the electrode contact due to a monopole (50 nA) at a given point in space. The isosurface (value of 257.5 μV), incorporated to enhance 3-dimensional visualization, is representative of the volume of recording sensitivity for the different electrodes. The encapsulation or edema sheath, when present, had a thickness of 20 μm . (C) Maps of percent change in sensitivity due to encapsulation (C₁) and edema (C₂) can be interpreted as the percent change in the recorded voltage amplitude as a function of source position. (D) Simulated waveforms generated by coupling the neuron model to each of the volume conductor models (default, encapsulation, and edema) showed an amplitude increase of $\sim 17\%$ when encapsulation was present and an amplitude decrease of $\sim 24\%$ when edema was present. (E) Experimental data (modified from Vetter et al., 2004) showed increases in the amplitude of signal and noise recordings that are consistent with model-based predictions of chronic encapsulation and/or removal of an acute edema condition.

challenging. However, one group did estimate experimentally the volume of recording sensitivity of a tetrode, a twisted-microwire electrode design using simultaneous intracellular and extracellular recording, and detailed histological processing (Henze et al., 2000). The recording sensitivity of the tetrode (peak-to-peak amplitudes of $\sim 60 \mu\text{V}$ recorded a distance of $50 \mu\text{m}$) was lower than the predicted sensitivity of the shank electrodes, and these observations are consistent with the conclusions from this study that a larger contact and the absence of the shank will yield lower recording amplitudes (Figs. 2–4).

We compared the recording amplitude as a function of neuron position (i.e. volume of recording sensitivity) for several contact sizes. All small contacts (from infinitesimal point to $1000 \mu\text{m}^2$) had the same volume of sensitivity (Fig. 4), i.e. for each contact the amplitude of recordings for a neuron $\sim 100 \mu\text{m}$ from the contact was $\sim 50 \mu\text{V}$. The large contact ($10\text{k} \mu\text{m}^2$) had a smaller volume of sensitivity ($50 \mu\text{V}$ recordings occurred at neuron-to-contact distance of $\sim 80 \mu\text{m}$), and a more uniform sensitivity than the smaller contacts (Fig. 4). These results indicate that a smaller contact size is preferred when non-uniform sensitivity is desirable, for example, when amplitude information is important for unit discrimination (Buzsaki, 2004). We also note here that the presence of the shank had the effect of shifting the volume of sensitivity to the side of the shank with the contact, and resulted in higher amplitude signals near the contact (Fig. 2), consistent with amplitude ranges

reported in the literature (Henze et al., 2000; Vetter et al., 2004).

4.4. Effect of changes in the local conductivity

Another objective of this study was to analyze the effects of changes in the electrical environment in the neighborhood of the electrode, as may occur with acute edema or chronic encapsulation. The perception in the literature is that encapsulation electrically isolates neurons from the recording electrode (Szarowski et al., 2003; Turner et al., 1999), and support for this idea comes from experimental data that demonstrate a reduction in the number of recordable units over time in a chronic preparation (Williams et al., 1999). However, additional data from the same (Williams et al., 1999) and other preparations (Vetter et al., 2004) have shown stability in chronic recordings, and even an increase in the amplitude of the signal and the noise over the first 4–6 weeks post-implant when encapsulation is expected to occur (Fig. 7 of Vetter et al., 2004; Szarowski et al., 2003; Turner et al., 1999). Contrary to the notion of electrical isolation, our results showed that incorporation of a simplified model of encapsulation (10–30 μm thick layer of increased resistivity) yielded an increase in the recording amplitude (Fig. 5), and the degree of signal amplification ($\sim 17\%$) appeared consistent with the experimental observations (Fig. 7 of Vetter et al., 2004). If encapsulation does cause an increase in the recording sensitivity of an electrode, observed decreases

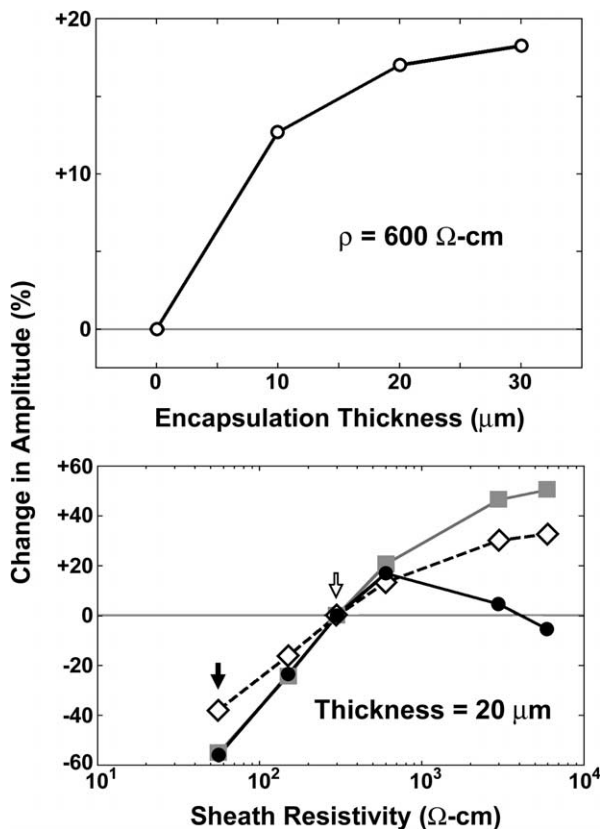


Fig. 6. Effects of encapsulation thickness and resistivity on signal amplitude. Percent change in peak-to-peak amplitude of the neural recordings as a function of encapsulation thickness (top) or sheath resistivity (bottom), relative to the default condition (no encapsulation or edema). The neuron is located at position (E) of Fig. 3. Thin gray horizontal lines in both plots represent 0% change. The sensitivity of recording amplitude to encapsulation thickness (top) was examined over the range [0, 30 μm] and the resistivity of the sheath was constant ($\rho = 600 \Omega \text{ cm}$). The sensitivity to sheath resistivity (bottom) was examined for resistivities lower than gray matter (representing edema) and resistivities higher than gray matter (representing encapsulation) (range = [56, 6000 $\Omega \text{ cm}$]) and the sheath thickness was constant (20 μm). The approximate resistivities of gray matter and cerebrospinal fluid are denoted by the open and solid arrows, respectively. The 3 traces represent peak-to-peak amplitude changes for the full neuron model (solid black line), the neuron model excluding dendritic currents in the sheath (solid gray line), and the amplitude change for a monopolar current 50 μm from the center of the contact (position E in Fig. 3) (dashed black line).

in the number of recordable units in some experiments might be explained by other mechanisms, such as movement of the neuron away from the contact (Fig. 4) or neurons becoming silent (Henze et al., 2000). An additional hypothesis for explaining the increased amplitude over time is that edema envelops the electrode acutely upon insertion, resulting in a decreased recording amplitude, and that over time the edemic condition is alleviated and the signal amplitude rises. The model results are consistent with this hypothesis, i.e. the model predicted that edema would result in a signal decrease (Fig. 5).

Thus, the increase in signal due to encapsulation predicted by the model offers one possible explanation for

experimental observations of a signal increase over time (Vetter et al., 2004). Note that an increase in signal amplitude is not inconsistent with experimental observations of signal degradation over time if there is a concurrent increase in noise amplitude (Vetter et al., 2004). Finally, it is reasonable to expect that small deviations in local conductivity in opposite directions will have opposite effects, and the results of the edema/encapsulation portion of this study are consistent with that notion.

We ran additional simulations to better understand the mechanisms of signal amplification in the case of encapsulation and signal reduction in the case of edema. In these simulations, a monopolar point current was placed 50 μm in front of the electrode contact, and the resistivity (ρ), the magnitude of the current-density ($|J|$), and the electric potential (Φ) were plotted (Fig. 7). Consistent with intuition, encapsulation yielded a decreased current-density in the neighborhood of the contact (Fig. 7B, D and E), and edema resulted in an increased current density (Fig. 7B, E and F). Note, however, that the change in the resistivity of the sheath (Fig. 7A) counteracts the change in current-density (compare Fig. 7A and B) per Ohm's law ($J\rho = -\text{Grad}(\Phi)$), and results in a net increase (Fig. 7C, G and H) or decrease (Fig. 7C, H and I) in electric potential due to encapsulation or edema, respectively. Finally, we note that when the encapsulation resistivity was sufficiently high ($\sim 6e5 \Omega \text{ cm}$), the recording amplitude began to decrease rapidly, presumably due to electrical isolation of the contact from the source.

4.5. Limitations of the computational model

Computational models are useful tools for understanding processes and refining methodologies, but they cannot exactly mimic experimental conditions, and assumptions and limitations must be considered during interpretation of the results. In this study, we first made the standard assumption that biological media can be considered resistive and linear in the context of neural recording (Plonsey, 1969; Bedard et al., 2004). The models used in this study were static, and did not include the double-layer capacitance known to exist at the electrode–electrolyte interface. Voltage measurements are necessarily taken with high impedance equipment, so we assumed that the effect of the electrode–electrolyte interfacial impedance is negligible. However, we cannot conclude that the effect is negligible and the effect should be quantified with next-generation models and experiments. Second, we assumed that the rat head could be modeled as concentric spheres. The comparison between models that did represent the head (Fig. 2, dashed gray lines) and that did not represent the head (Fig. 2, solid gray lines) indicates that the results are not very sensitive to the geometry of the head model. Third, the effects of noise were not considered in this initial study, and an important subsequent step is to incorporate models of

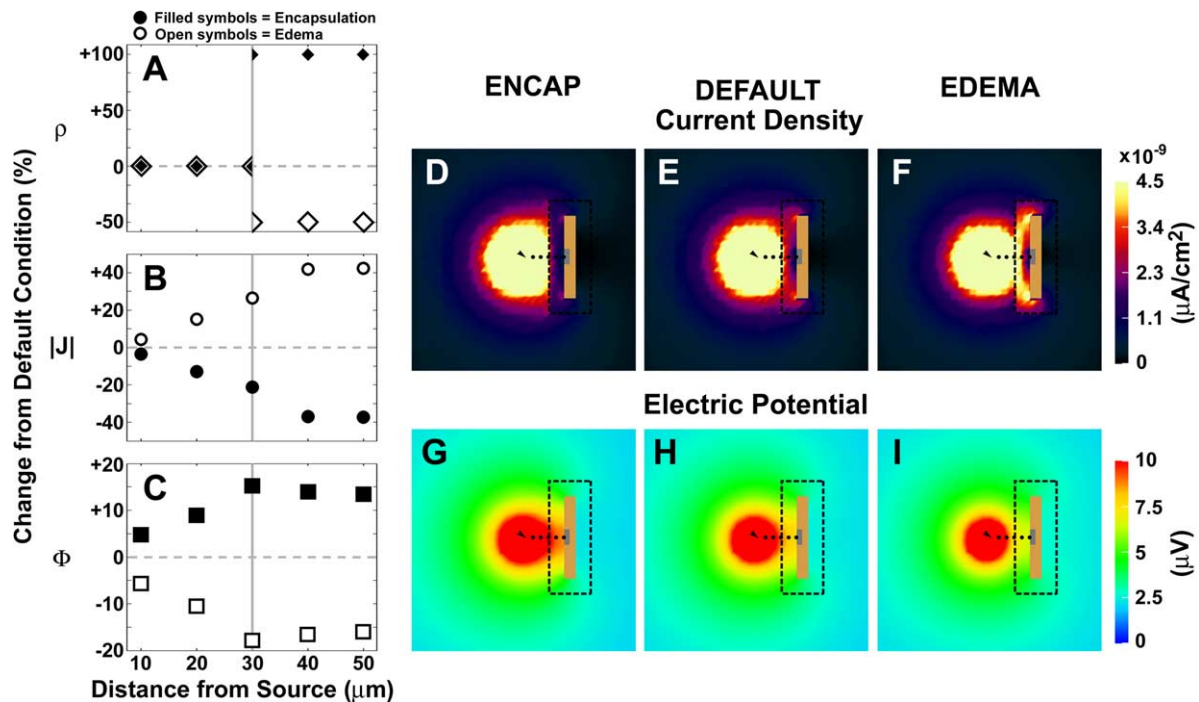


Fig. 7. Influence of local electrical inhomogeneities on neural recordings. Thin sheaths ($20\ \mu\text{m}$) of encapsulation ($\rho=600\ \Omega\ \text{cm}$) or edema ($\rho=150\ \Omega\ \text{cm}$) generate opposite effects on local current density ($|J|$) and potential (Φ). (A) Resistivity changes near the electrode for encapsulation (filled symbols) or edema (open symbols) changed the local current density (B) and potential (C) caused by a monopolar current source $50\ \mu\text{m}$ from the contact. False-color maps of the current density (D–F) and potential (G–I) are shown for encapsulation (D, G), default condition (absence of a sheath) (E, H), and edema (F, I) scenarios. The source location, recording points, and encapsulation border are represented by the arrow, dots, and dashed outline, respectively. Encapsulation resulted in a decreased current density, but an increased potential, and edema resulted in the opposite effect. These results are related to the product of ρ and J ($-\text{Gradient}(\Phi)=\rho J$), where the change in ρ impacted Φ more than the opposite change in J .

non-physiological and physiological noise into the existing model. Noise that is dependent on contact size, such as thermal noise (Huigen et al., 2002), will be particularly important when considering optimization of contact size. Fourth, the model of encapsulation consisted of a single, $20\ \mu\text{m}$ thick, electrical domain, when in reality it consists of a number of cells around and adhered to the electrode (Turner et al., 1999). It is possible that a model that incorporates a more realistic microstructure of encapsulation, particularly near the contact, could affect the results, although we expect that the trends would be similar to those reported here. Also, in most simulations in this study, dendritic sources were permitted to exist inside the encapsulation layer (7 of 400 dendritic current sources within $20\ \mu\text{m}$ of shank). It is not clear if this occurs physiologically, but neural recordings were highly sensitive to sources within the encapsulation (Fig. 6, bottom). Finally, small contact sizes ($\leq 1000\ \mu\text{m}^2$) yielded comparable recordings for neurons $\geq 50\ \mu\text{m}$ from the electrode. Our model was designed to predict the spatial extent of recording with various contact designs, and we did not address recordings with neurons $\leq 50\ \mu\text{m}$ from the electrode contact. But, it should be noted that more pronounced differences between the recordings with various contact dimensions would be expected when neurons are especially close to the contact (Buitenweg et al., 2003).

In conclusion, the results of this modeling study were consistent with several experimental observations and extend our understanding of neural recording, and particularly neural recording with silicon microelectrodes. The results indicated that small electrode contacts ($\leq 1000\ \mu\text{m}^2$) have comparable volumes of recording sensitivity ($\sim 100\ \mu\text{m}$) (Fig. 4), and that the volume of sensitivity is less uniform for small electrodes than with large electrodes. Further, the model predicted that edema reduced signal amplitude ($\sim 24\%$) and that encapsulation increased the signal amplitude ($\sim 17\%$). This model-based result encourages further experimental evaluation of the effect of encapsulation and coatings on the amplitude of neural recordings. The results of this study provide the foundation for the development of theoretically optimal microelectrode designs that will improve the quality of brain-machine interfaces for clinical applications.

Acknowledgements

The authors gratefully acknowledge time and effort contributed by Amanda Adams, and thank Justin Williams and Kip Ludwig for helpful discussion. This work was supported by a grant from the Ohio Biomedical Research and Technology Transfer Partnership.

References

- Bedard C, Kroger H, Destexhe A. Modeling extracellular field potentials and the frequency-filtering proper ties of extracellular space. *Biophys J* 2004;86(3):1829–42.
- Buitenweg JR, Rutten WL, Marani E. Geometry-based finite-element modeling of the electrical contact between a cultured neuron and a microelectrode. *IEEE Trans Biomed Eng* 2003;50(4):501–9.
- Buzsaki G. Large-scale recording of neuronal ensembles. *Nat Neurosci* 2004;7(5):446–51.
- Csicsvari J, Henze DA, Jamieson B, Harris KD, Sirota A, Bartho P, Wise K D, Buzsaki G. Massively parallel recording of unit and local field potentials with silicon-based electrodes. *J Neurophysiol* 2003;90(2):1314–23.
- Cui X, Lee VA, Raphael Y, Wiler JA, Hetke JF, Anderson DJ, Martin DC. Surface modification of neural recording electrodes with conducting polymer/biomolecule blends. *J Biomed Mater Res* 2001;56(2):261–72.
- Franconi F, Lemaire L, Marescaux L, Jallet P, Le Jeune JJ. In vivo quantitative microimaging of rat spinal cord at 7T. *Magn Reson Med* 2000;44(6):893–8.
- Grill WM, Mortimer JT. Electrical properties of implant encapsulation tissue. *Ann Biomed Eng* 1994;22(1):23–33.
- Haueisen J, Tuch DS, Ramon C, Schimpf PH, Wedeen VJ, George JS, Belliveau JW. The influence of brain tissue anisotropy on human EEG and MEG. *Neuroimage* 2002;15(1):159–66.
- Helmholtz HLF. Ueber einige gesetze der vertheilung elektrischer strome in körperlichen leitern mit anwendung auf die thierisch-elektrischen versuche. *Ann Physik Chemie* 1853;89(211–233):354–77.
- Henze DA, Borhegyi Z, Csicsvari J, Mamiya A, Harris KD, Buzsaki G. Intracellular features predicted by extracellular recordings in the hippocampus in vivo. *J Neurophysiol* 2000;84(1):390–400.
- Hines ML, Carnevale NT. simulation environment. *Neural Comput* 1997;9(6):1179–209.
- Holt GR, Koch C. Electrical interactions via the extracellular potential near cell bodies. *J Comput Neurosci* 1999;6(2):169–84.
- Huigen E, Peper A, Grimbergen CA. Investigation into the origin of the noise of surface electrodes. *Med Biol Eng Comput* 2002;40(3):332–8.
- Kennedy PR, Kirby MT, Moore MM, King B, Mallory A. Computer control using human intracortical local field potentials. *IEEE Trans Neural Syst Rehabil Eng* 2004;12(3):339–44.
- Liu CH, D'Arceuil HE, de Crespigny AJ. Direct CSF injection of MnCl₂ for dynamic manganese-enhanced MRI. *Magn Reson Med* 2004;51(5):978–87.
- Mainen ZF, Joerges J, Huguenard JR, Sejnowski TJ. A model of spike initiation in neocortical pyramidal neurons. *Neuron* 1995;15(6):1427–39.
- Mainen ZF, Sejnowski TJ. Influence of dendritic structure on firing pattern in model neocortical neurons. *Nature* 1996;382(6589):363–6.
- Nicolelis MA, Chapin JK. Controlling robots with the mind. *Sci Am* 2002;287(4):46–53.
- Ogiue-Ikeda M, Kawato S, Ueno S. The effect of repetitive transcranial magnetic stimulation on long-term potentiation in rat hippocampus depends on stimulus intensity. *Brain Res* 2003;993(1–2):222–6.
- Plonsey R. Bioelectric phenomena. New York: McGraw-Hill; 1969.
- Rall W. Electrophysiology of a dendritic neuron model. *Biophys J* 1962;2(2):145–67.
- Rush S, Driscoll DA. EEG electrode sensitivity—an application of reciprocity. *IEEE Trans Biomed Eng* 1969;16(1):15–22.
- Serruya M, Caplan A, Saleh M, Morris D, Donoghue J. The BrainGate pilot trial: building and testing a novel direct neural output for patients with severe motor impairment. *Soci Neurosci Abstr* 2004;19022.
- Szarowski DH, Andersen MD, Retterer S, Spence AJ, Isaacson M, Craighead HG, Turner JN, Shain W. Brain responses to micro-machined silicon devices. *Brain Res* 2003;983(1–2):23–35.
- Taylor DM, Tillery SI, Schwartz AB. Direct cortical control of 3D neuroprosthetic devices. *Science* 2002;296(5574):1829–32.
- Thorsen F, Erslund L, Nordli H, Enger PO, Huszthy PC, Lundervold A, Standnes T, Bjerkvig R, Lund-Johansen M. Imaging of experimental rat gliomas using a clinical MR scanner. *J Neurooncol* 2003;63(3):225–31.
- Turner JN, Shain W, Szarowski DH, Andersen M, Martins S, Isaacson M, Craighead H. Cerebral astrocyte response to micromachined silicon implants. *Exp Neurol* 1999;156(1):33–49.
- Vetter RJ, Williams JC, Hetke JF, Nunamaker EA, Kipke DR. Chronic neural recording using silicon-substrate microelectrode arrays implanted in cerebral cortex. *IEEE Trans Biomed Eng* 2004;51(6):896–904.
- Williams JC, Rennaker RL, Kipke DR. Long-term neural recording characteristics of wire microelectrode arrays implanted in cerebral cortex. *Brain Res Brain Res Protoc* 1999;4(3):303–13.